Seismic Noise by Wind Farms: A Case Study from the VIRGO Gravitational Wave Observatory, Italy.

Gilberto Saccorotti[1*], *Davide Piccinini*[1], *Léna Cauchie*[1,2], *and Irene Fiori*[3]

[1] (*corresponding author)
Istituto Nazionale di Geofisica e Vulcanologia, Sezione di Pisa
Via U. della Faggiola, 32 - 56126 PISA (I)
Tel +39 050 8311960
saccorotti@pi.ingv.it

[2] University College of Dublin, School of Geological Sciences - Dublin (Ireland)
lena.cauchie@gmail.com

[3] European Gravitational Observatory, Cascina, Pisa (Italy)
irene.fiori@ego-gw.it

Abstract

We present analyses of the noise wavefield in the vicinity of VIRGO, the Italy-France gravitational wave observatory located close to Pisa, Italy, with special reference to the vibrations induced by a nearby wind park. The spectral contribution of the wind turbines is investigated using (i) on-site measurements, (ii) correlation of spectral amplitudes with wind speed, (iii) directional properties determined via multichannel measurements, and (iv) attenuation of signal amplitude with distance. Among the different spectral peaks thus discriminated, the one at frequency 1.7 Hz has associated the greatest power, and under particular conditions it can be observed at distances as large as 11 km from the wind park. The spatial decay of amplitudes exhibits a complicate pattern, that we interpret in terms of the combination of direct surface waves and body waves refracted at a deep ($\approx$ 800 m) interface between the plio-pleistocenic marine, fluvial and lacustrine sediments and the Miocene carbonate basement. We develop a model for wave attenuation which allows determining the amplitude of the radiation from individual turbines, which is estimated on the order of 300-400 $\mu m s^{-1}/\sqrt{Hz}$ for wind speeds over the 8-14 m/s range. On the base of this model, we then develop a predictive relationship for assessing the possible impact of future, project wind farms.

1 Introduction

Several detectors are nowadays operative to reveal the tiny space-time ripples which, according to Einstein's theory of general relativity, are expected in association with astrophysical processes, like supernova explosions, coalescence of binary systems, spinning neutron stars.

A class of these gravitational waves detectors (Saulson, 1994) works on the principle of the Michelson interferometer;

detectors of this kind are GEO-600 in Germany, LIGO in USA, TAMA in Japan, and VIRGO in Italy (see *The Virgo collaboration, Virgo Final Design 1997 VIR-TRE-DIR-1000-13* available at https//pub3.ego-gw.it/itf/tds). Established under an Italy-France cooperative effort (EGO; European Gravitational Observatory), VIRGO is located south of Pisa, about 15 km onshore the central-northern Thyrrenian Coast (Fig. 1). The VIRGO laser interferometer consists of two 3-km-long orthogonal arms oriented $N20°E$ and $N70°W$ departing from a central building (CB). The end mirrors of the interferometer are located at the extremities of the two arms, hereinafter referred to as North- and West-End (NE and WE, respectively). Multiple reflections between these mirrors extend the effective optical length of each arm up to 120 kilometers, thus allowing for sensitivity to spatial strains on the order of $\approx\ 10^{-22}$ over the 10 Hz–10000 Hz frequency range. In order to achieve such extreme sensitivities, the interferometer exploits the most advanced techniques in the field of high power ultrastable lasers, high reflectivity mirrors, and seismic isolation systems (Acernese et al., 2010*a*). Nonetheless, intense low frequency ground vibrations might overcome the isolation system and deteriorate the detector performances. A major concern is that low frequency (1 Hz–10 Hz) periodic disturbances might match and excite the low frequency modes of the isolation systems, seriously compromising its functionality. Another concern for VIRGO is the noise associated to the tiny fractions of light which exits the interferometer main beam path and are then scattered back by external, seismically excited surfaces (Vinet et al., 1996; Acernese et al., 2010*b*).

By mid 2008, a wind park composed by four, 2MW turbines was installed at some 6 km East of VIRGO's NE (Fig. 1). After then, plans were submitted to local authorities for (i) adding three additional turbines to the existing wind park, and (ii) installing a new, 7-turbine wind park at a site located about 5 km west of VIRGO's WE. As a consequence, EGO asked to the italian Istituto Nazionale di Geofisica e Vulcanologia (INGV hereinafter) to conduct a noise study aiming at (i) verifying properties and intensity of the vibrations produced by the present aerogenerators, with the ultimate goal of (ii) assessing the possible impact of the project wind parks.

Wind turbines are large and vibrating cylindrical towers strongly coupled to the ground through massive concrete foundation, with rotating turbine blades generating low-frequency acoustic signals.

Vibrations depict a complex spectrum, which includes both time-varying frequency peaks directly related to the blade-passing frequency, and stationary peaks associated with the pendulum modes of the heavy rotor head and tower, and to flexural modes of the tower.
These disturbances propagate via complex paths including directly through the ground or principally through the air and then coupling locally into the ground. Though weak, such vibrations may be relevant once compared to the local levels of seismic noise. Schofield (2001) found that the intense low frequency seismic disturbances from the Stateline Wind Project (Washington-Oregon, USA) were well above the local seismic background till distances of $\approx$ 18 km from the turbines. Similar distance ranges were found by Styles et al. (2005), who analysed the possible influence of a project wind park at Eskdalemuir (Scotland), in the vicinity of the UK Seismic Array. Fiori et al. (2009) studied the seismic noise generated by a wind park in proximity of the GEO-600 interferometric antenna (Germany), and observed the signal from the turbines till distances of about 2000 m.

In this work we present the results from seismic noise analysis in the vicinity of VIRGO, with special reference to the action of the wind park. The paper is structured into four parts. In the first part (Sections 2-3), we describe the geological setting of the study area and describe the data acquisition procedures. We then describe (Section 4) the spectral characteristics of the noise wavefield, and their relationships with human activities and the wind field. In the third part (sections 5 and 6), we use small- and large-aperture array deployments to investigate the directional properties of the noise wavefield and its amplitude decay with distance from the windfarm. In the last part (Section 7) we propose an attenuation model involving the combination of direct cylindrical waves propagating at the surface, and body waves refracted at a deep (800 m) lithological interface. This attenuation law is eventually used for establishing a predictive relationship for assessing the range of seismic amplitudes which are expected in association with narrow-band, shallow sources of noise.

2 The Study Area

EGO-VIRGO is located in the southernmost portion of the Lower Arno river, a Neogenic-Quaternary back-arc basin, which formed in the Middle-Miocene, during the Northern Thyrrenian Basin extensional phases (Fanucci et al., 1987; Patacca et al., 1990). This tectonic depression is bounded by the *Monti Pisani* to the north and by other smooth relief to the south (*Monti Livornesi*). The tectonic and climatic pulses during the Miocene allowed marine and continental deposits to overlay the Mesozoic bedrock and the metamorphic Tuscan Unit, previously collapsed along a set of NW striking normal faults (Cantini et al., 2001). As a consequence, the top of the carbonatic bedrock deepens from depths of ≈ 700 m to depths of ≈ 2500 m as one moves from the eastern to the western sector of the plain (Mariani and Prato, 1988; Della Rocca et al., 1988). The shallow geology (up to depths of ≈ 60 m) is well documented by a large number of boreholes and surveys, which overall confirm the stratigraphic settings previously described by several authors (e.g., Mazzanti and Rau, 1994; Stefanelli et al., 2008). According to these studies, the deposition due to the glacial activity and the eustatic changes during Pleistocene fills up the basin with four main layers:

i) conglomerates (Conglomerates of the Arno River and Serchio from Bientina) attributed to the Wurm II inter-glacial period (60 ky - 40 ky before present);

ii) deep mud and fluvio-lacustrine deposits; iii) sands; iv) shallow mud and fluvio–lacustrine clays (Grassi and Cortecci, 2006).

3 Data Acquisition and Processing

Our seismic survey had the main goal of discriminating which components of the noise wavefield are likely due to the action of the wind generators, in turn determining how these signals propagate and attenuate.

To attain these objectives, we deployed the instruments according to different, time-varying configurations, designed in order to provide the best resolution for both directional and attenuation measurements over a wide frequency band and distance range. In total we used 14 seismic stations, three of which were kept fixed at the same location throughout the duration of the survey (sites 1078, 7148 and 931E in Fig. 1), while other three were used for short-duration measurements of site effects via H/V spectral ratios (not described in this paper).

Our instruments consisted of nine RT130- and five 72A-type recorders from REFTEK, each synchronised to the GPS time signal. All mobile stations used Lennartz LE3D-5s, three-component velocimeters exhibiting a flat velocity response over the 0.2-40 Hz frequency band, while two of the three reference sites (1078 and 7148) were equipped with Guralp CMG40, three-component broad-band seismometers with flat velocity response over the 0.025-50 Hz frequency band. For all these instruments sampling rate was set at 125 samples/second/channel. Complementing these data are recordings from two two FBA ES-T EpiSensor accelerometers and a further CMG40 velocimeter located at VIRGO's vertexes and central building, respectively. These latter instruments are part of VIRGO's internal monitoring network, and are acquired at a rate of 1 KHz and successively down-sampled at 50 samples/second/channel.

Data acquisition started on the 26th of October and terminated on the 17th of November, 2009.

Before the data collection, we performed accurate huddle tests between all the possible combinations of recorder/sensor pairs using either noise samples or teleseismic signals to verify the sameness of the amplitude response of the different instruments over the whole frequency band of sensitivity. All the spectra presented throughout the following are either velocity or displacement amplitude spectral densities, derived from the square root of Power Spectral Density (PSD) estimates, calculated via Welch's (1967) method. Wind data are from an anemometer located atop VIRGO's control building, recording wind speed and direction at a rate of 1 datum every 10 s.

4 Seismic Noise in proximity of the Wind Park

4.1 Spectral Properties

Seismic noise in proximity of the wind park exhibits a typical weekly and daily pattern (the 8-hr workday, for example), as depicted by the spectrogram of Figure 2.

Spectra of human noise span the 1 Hz-20 Hz frequency band, as shown in Figure 3, where we compare spectra taken during a day and night intervals in absence of wind. In general, spectra taken at day time are an amplified version of those collected during the night, indicating that no monochromatic signals are generated by human activities.

On the other side, the nightly spectra depict several narrow spectral peaks which origin is not likely related to anthropic noise (e.g., the peak at frequency $\approx$ 1.7 Hz on the NS component, and narrow peaks at frequencies $\approx$ 3 Hz, 4 Hz, 5.5 Hz, 7 Hz on the EW component). As it is shown in the rest of the paper, the peak at frequency $\approx$ 1.7 Hz of the NS component is the one which assumes the greatest relevance to the purpose of this study.

4.2 Noise amplitude and wind speed

Rows of the spectrogram in Figure 2 are time series of the narrow-band noise amplitude, that we cross-correlate against the contemporaneous time series of wind speed in order to verify whether particular spectral lines are coupled to the action of the wind. The frequency-dependent maxima of the cross-correlation function and associated lag times are shown in Figures 4a and 4b for the NS component of motion. Noise exhibits a good correlation with wind speed at several discrete frequencies, centered at around 0.45, 1.7, 3.5, 4.5 Hz.

An example of such correlation is shown in Figure 4c where the time series of noise amplitude at frequency 1.7 Hz is compared with the chronogram of wind speed. At frequencies above 1 Hz, the correlation peaks of Figure 4a occur at zero lag (Fig. 4b); in other words, noise amplitude grows contemporaneously to the increase of wind speed.

On the contrary, noise amplitude at frequency 0.45 Hz is delayed by several hundred minutes with respect to the wind intensity, suggesting that marine microseism is the most likely origin for the seismic noise at that particular frequency.

Correlation of seismic noise amplitude with wind speed is well documented by numerous previous studies (e.g., Withers et al., 1996, and references therein). All these works indicate however that an increase in wind speed affects seismic noise over a wide frequency band (e.g., 1 Hz-50 Hz). Our narrow-band correlations are therefore suggestive of an harmonic source which is itself excited by the action of the wind.

4.3 Noise from an individual turbine

Figure 5 illustrates the spectrogram for the vertical component of ground velocity recorded in close proximity of an aerogenerator, and encompassing a switch-on of the turbine. While the turbine is stopped, we recognise a few transients overimposed to a continuous radiation at frequency 0.45 Hz. We attribute this energy to the eigen-oscillation of the tower, which is occasionally excited by adjustments of the nacelle orientation. The switch-on of the turbine is well recognised at about 3000 s into the recording, and it is marked by (i) a few steady spectral lines, the most important of which are at frequencies of 0.45 Hz and 1.7 Hz, and (ii) time-varying peaks (gliding spectral lines), at frequencies of about 0.3 Hz, 0.6 Hz, 0.9 Hz,... up to 20 Hz and above. The time stationarity of the former peaks indicates that these are likely due to the different modes of oscillation of the tower. Conversely, the gliding spectral lines are attributed to the rotation of the blades which complete period of revolution varies within the 3-10 s range as a function of wind speed and nacelle orientation. Figure 6 compares spectra from beneath the turbine (taken at low wind speeds) with not-contemporaneous spectra observed at the reference site 931E during a 1-hour-long period of stong wind. The two sets of spectra are markedly different, and the only common peak is found at the Z and NS components of motion, at frequency 1.7 Hz. This suggests that either the other peaks that we found to correlate clearly with wind speed (e.g., 3.5, 4.5 Hz...) are not related to the action of the wind park, or that path effects, and the combination of waves radiated from individual turbines, modify severely the spectral composition of the seismic noise as it propagates away from the wind park.

As a consequence, beneath-turbine measurements cannot be taken as representative of the overall wind park noise as observed in the far field. The next two sections are thus dedicated to finding indirect evidences for determining the noise spectral components which are actually due to the action of the wind park.

5 Directional Properties and Wavetypes

In this section we use a dense, 2-D array deployment installed about 480 m from the closest turbine to investigate the composition of the noise wavefield around the wind park. Under the plane-wave approximation, we use inter-station delay times measured via cross-correlation to derive the two component of the horizontal slowness vector and hence apparent velocity and backazimuth for waves impinging at the array (Del Pezzo and Giudicepietro, 2002). Multichannel data streams are first passed through a bank of 0.2-Hz-wide band-pass filters spanning the 0.1-5.1 Hz frequency band; for each frequency band, inter-station cross correlations are calculated using non-overlapping, 600-s-long windows of signal, thus allowing for a time- and frequency-dependent estimates of the kinematic properties of the noise wavefield. We decided to use such long time windows since we noted correlation estimates to become stable for time windows longer than $\approx$ 500 s.

The results, shown in Figure 7, clearly indicate that most of the energy at frequency above 1 Hz propagates from directions which are compatible with the wind park (backazimuths between 90° and 110°). Conversely, waves at frequencies below 1 Hz mostly come from the coast (i.e., backazimuths pointing to West), confirming that marine microseism is the most powerful source over this particular frequency range.

Our measurements also indicate a marked dispersion, indicating a dominance of surface waves. Phase velocities range from 1000-2000 m/s below 1 Hz, to 100-200 m/s at frequencies above 2 Hz. These values are consistent with those listed by Castagna et al. (1985) for shear waves propagating in saturated, unconsolidated sediments. At frequency 1.7 Hz, particle motions at the array site are mostly horizontal, and oriented N-S (i.e., perpendicularly to the direction of propagation), thus suggesting a dominance of Love waves.

6 Attenuation with distance

Figure 8 illustrates the spatial decrease of spectral amplitudes as a function of distance from the wind park. Measurements are taken during a windy night (wind speed $\approx$ 50 km/h), for which we do expect low intensity of human sources and high radiation from the wind turbines.

Several out of the frequency peaks which correlate well with wind speed (e.g., 1.7, 3.5, 4.5 Hz on the NS component) attenuate as one goes farther from the wind park, thus reinforcing the hypothesis that these peaks are due to the action of the turbines. In particular, the peak at frequency 1.7 Hz is clearly observed also at VIRGO's WE, about 11 km from the energy plant.

For this particular frequency, the decay of spectral amplitude with increasing distance from the source exhibits a complicate pattern (Fig. 8b). In particular, we observe a marked change in the amplitude decay rate for source-to-receiver distances on the order of 2500-3000 m.

A simplified propagation model explaining the two different attenuation rates involves the combination of direct surface waves, and body waves propagating along deeper paths characterised by higher velocities and quality factors.

In this model, if we assume an isotropic source located at the free surface, the amplitude of the surface waves $A_D(f,r)$ scales with distance r according to a general attenuation law for cylindrical waves (e.g., Del Pezzo et al., 1989):

$$A_D(f,r) = \frac{A_0}{\sqrt{r}} e^{-\frac{\pi f r}{Q_0 v_0}} \tag{1}$$

where A_0 is the seismic amplitude at the source, f is the frequency, and

(Q_0, v_0) are the quality factor and surface-wave velocity of the shallowest layer,respectively,.

As for the body waves, we simplify their propagation in terms of head waves refracted at a deep ($\approx$ 800 m) interface between the shallow plio-pleistocenic sediments and the miocene carbonates (Fig. 9). The down- and up-going ray segments of these waves traverse an 800-m-thick layer of average Quality Factor and shear-wave velocity (Q_1, v_1), respectively, and are continuosly refracted at the interface with an half-space of quality factor and velocity (Q_2, v_2). Neglecting the short propagation paths throughout the shallowest layer, the attenuation with distance of these body waves is thus described by the relationship:

$$A_R(f,r) = A_0(2r_1 + r_2)^{-n} e^{\frac{-2\pi r_1 f}{Q_1 v_1} - \frac{\pi r_2 f}{Q_2 v_2}} \quad (2)$$

where n is the geometrical spreading coefficient which, for body waves, is expected to take unit value.

Thus, for an observer recording the signal from N turbines which vibrate with the same amplitude A_0 and are located at distances $r_i, i = 1 \ldots N$, the amplitude is given by the sum of eqs. (1) and (2):

$$A_T(f) = A_0 \sum_{i=1}^{N} (A_D(f, r_i) + A_R(f, r_i)) \quad (3)$$

remembering however that the A_R term (eq. 2) is not defined for horizontal distances r shorter than the critical distance.

Equation 3 is based on the critical assumptions that (i) each turbine radiates a signal of the same amplitude; (ii) these signals propagate in phase, thus constructively interfering throughout their paths, and (iii) the energy is equally parted into surface- and body-wave raypaths.

The free parameters in equation (3) are the velocities and quality factors $v_i, Q_i \quad (i = 0, \ldots 2)$ of the two layers and the halfspace, the geometrical spreading coefficient n of the body head waves, and the amplitude A_0 of the radiation from each individual turbine. The depth to the top of the carbonate basement h is rather well constrained by well-log data, and as specified above it is assumed to take the value of 800 m.

For fitting eq.(3) to data, we first consider a sample set of amplitude vs. distance measurements obtained over 1-hour-long recording at 14, 3-component stations. For these signals, we average the amplitude spectral densities over a 0.1 Hz-wide frequency band encompassing the reference frequency of 1.7 Hz, and eventually obtain three-component amplitudes from the quadrature sum of spectra derived at the individual components of ground motion.

The fit is conducted using an exhaustive grid search in which all the free parameters in eq.(3) are allowed to vary over appropriate ranges. For A_0 and n we used 11 values spanning the [10–1000] $\mu m s^{-1}/\sqrt{Hz}$ and [0.5–1] ranges, respectively. The three $Q_i \times v_i \quad (i = 0 \ldots 2)$ products were instead allowed to vary over an $11 \times 11 \times 11$ grid spanning the [3000,5000], [10000,80000] and [100000,200000] m/s intervals, respectively. These ranges encompasses S-wave velocity and quality factor values which are expected in association with the shallow geology of the site (e.g., Campbell, 2009; Castagna, 1985). For each combination of these parameters, we then calculate the L_1 misfit function:

$$L_1(\mathbf{m}) = \sum_{i=1}^{N_{obs}} |A^{obs}(r_i) - A^{pre}(r_i)| \tag{4}$$

where $\mathbf{m}$ is a model vector containing the parameters $(A_0, n, Q_0V_0, Q_1V1, Q_2V_2)$, and A^{obs}, A^{pre} are the observed amplitudes and those predicted in the sense

of eq.(3). From this procedure, we noted that the misfit function (eq. 4) is mostly sensitive to the source amplitude and body-wave spreading coefficient. Therefore, we assigned to seismic velocities and quality factors the values reported in Figure 9, and inverted amplitude observations only for the spreading coefficient of body waves and the amplitude at the source.
The inversion was separately applied to amplitude data taken from twenty, 1-hour-long interval of noise recorded by different network geometries, at distances from the barycenter of the wind park ranging from 1200 m to $\approx$ 11000 m. For each set of measurements, we only considered stations for which the peak at 1.7 Hz was clearly visible. Best–fitting values of A_0 and n were sought over a 21×21 regular grid spanning the same intervals mentioned above.

Figure 10 shows the L_1 error function from a sample data set, and the comparison between the observed amplitudes and those predicted on the basis of the minimum-norm model.

The sample error function of Figure 10a indicates a clear correlation between A_0 and n. Nonetheless, results from the whole set of inversions depict narrow distributions, thus supporting the overall robustness of the estimates. In fact, mean values and $\pm$ 1σ uncertainties for the A_0/A_{rif} ratio (where A_{rif} is the amplitude at reference site 931E) and the spreading coefficient n are 29.9 ± 1.9 and 0.70 ± 0.04, respectively.

The geometrical spreading coefficient of head waves is sensitively smaller than the unit value which is expected for body waves. This occurrence is likely due to the fact that our simplified model assumes that the source radiates isotropically, in turn neglecting the additional conversion to surface waves as body waves impinge at the earth's surface.

7 Predictive Relationship

The points discussed above allow establishing a predictive relationship for assessing the effects of future wind plants with custom turbine configuration. As a first step, we use the results from the inversion of amplitude data to convert the seismic amplitude observed at the reference site to the radiation amplitude at unit distance from a single turbine.
In order to relate these amplitudes to the wind speed, we consider that the energy in a volume of air goes as the square of its velocity, and that the volume that pass by the turbine per unit time increases linearly with wind velocity.

Thus, the available power P at an individual turbine goes as the cube of the wind velocity W: $P \propto W^3$.

By further assuming that the power in the seismic signal is proportional to the wind power available to the turbine, it turns out that the signal amplitude goes as the wind velocity to the 3/2 power (Schofield, 2001; Fiori et al., 2009). We thus plot the single-turbine amplitudes against the wind speed for the entire observation period, and fit these data with a power law in the form:

$$A_s = c + a \cdot W^{\frac{3}{2}} \tag{5}$$

where A_s is the amplitude spectral density of the ground velocity (in $ms^{-1}/\sqrt{Hz}$) at unit distance from a single turbine, and W is the wind speed in m/s (Fig. 11). The best-fitting parameters are a=2.13×10$^-7$ $Hz^{-0.5}$ and $c = 1.40 \times 10^-6$ $ms^{-1}Hz^{-0.5}$. The fit is not very well constrained, likely due to a combination of several causes, such as: (i) contamination of the seismic signal by additional noise sources, and (ii) difference of the wind field between VIRGO's anenometer and the wind park.

Keeping these limitation in mind, one can substitute the A_0 of eq. (3) with the right-hand side of eq. (5), thus deriving the expected spatial distribution of ground vibration amplitudes as a function of wind speed, for any custom configuration of wind turbines. Once a robust statistics of wind speed will be available, these data will eventually allow to derive 'shake maps' describing the probability of exceeding given ground motion amplitudes throughouit the study area.In this application, moreever, it must be considered that the wind speed measured at VIRGO's anenometer (placed at $\approx$ 10 m height) is expected to be sensitively smaller than that at the blades' elevation (60-100 m).

8 Discussion and Conclusion

In this paper we analysed the seismic noise wavefield in the vicinity of the VIRGO gravitational wave observatory (Cascina, Pisa - Italy), with special reference to the action of a nearby wind park composed by four, 2 MW turbines. Using stations deployed at distances ranging between $\approx$ 1200 m and $\approx$ 11,000 m from the barycenter of the wind park, we obtained recordings of the noise wavefield over a wide range of site condition and epicentral ranges. We noted that path effects modify significantly the source spectrum, implying that beneath-turbine measurements are not fully indicative of the effective contribution of the wind park to the far–field ground vibration spectra. Therefore, the spectral components of the noise wavefield likely due to the action of the wind park had to be discriminated on the basis of indirect evidences, including: (i) Correlation of narrow-band noise amplitude with wind speed; (ii) Directional properties, and (iii) Attenuation with increasing distance from the wind park.

Basing on these results, we individuated several frequency bands likely due to the action of the wind park. Among these, the most energetic is that at frequency 1.7 Hz which, under particular conditions (i.e., low cultural noise and strong wind) can be clearly observed at epicentral distances as large as 11 km.

At this particular frequency, waves depict a complicate pattern of attenuation with distance, characterised by a marked decrease in the decay rate for ranges larger than 2500–3000 m.

We interpreted this pattern in terms of a simplified propagation model involving the combination of direct, cylindrical waves and body head waves continuosly refracted at a deep ($\approx$ 800 m) interface separating the shallow marine-lacustrine sediments from the carbonate basement. This model is based on several simplifying assumptions, including: (i) Seismic energy is equally parted into surface and head body waves, and no other wave types and/or wave conversions are allowed, and (ii) Site effects are negligible.

By further assuming that (i) Each turbine radiates the same amount of energy; (ii) Signals from individual turbines sum constructively, (iii) the velocity structure of the propagation medium is laterally-homogeneous, and (iv) Local amplification effects are negligible, we thus defined a model relating the seismic amplitude recorded at a given distance to the radiation of each individual turbine.

Assumption (ii) above is likely to provide an over-estimation of the radiation amplitude from individual turbines. A more realistic estimates should consider that the turbines are not all in phase and neither are they operating at exactly the same frequency, because of the slight possible variations in rotation speed and wind conditions across the farm. These are quasi-random sources and therefore add in quadrature, and not linearly as previously assumed. Therefore 100 turbines are 10 times as noisy as 1, not 100 times. Thus, since we're dealing with a park composed by 4 turbines, the above consideration would imply scaling the estimated single-turbine amplitudes by about a factor 2, which is probably not so relevant once compared to the assumptions reported at points (iii) and (iv) above (i.e., site and path effects).

Separately, we also found a relationship between wind speed and noise amplitude, which is reasonably well-fitted by a power law. Therefore, these two pieces of information allow us to build a predictive relationship linking wind speed with expected noise amplitude for any custom configuration of turbines. This latter argument will permit, given a robust statistics of wind speed, to assess the probabilities of exceeding an arbitrary noise amplitude threshold at any site of interest within the study area, as a consequence of present or project wind parks.

9 Data and Resources

All data used for this study are property of the EGO Consortium and cannot be released to the public.

10 Acknowledgements

Thoughtful revisions from Martin C. Chapman, Salvatore de Lorenzo and an anonymous reviewer greatly contributed to improving the quality of the

manuscript. The research was fully supported by the EGO Consortium. Thomas Braun, Riccardo Azzara, Nicola Piana Agostinetti, Chiara Montagna and Luciano Zuccarello participated to the field survey. Federico Paoletti provided superb logistic assistance during the data aquisition. Finally, we are grateful to Jacques Colas, whose constructive criticisms greatly stimulated the conduction of the research.

11 References

Acernese, F., et al. (2010a) Measurements of Superattenuator seismic isolation by Virgo interferometer. *Astrop. Phys.*, **33** , 182-189.

Acernese, F., et al. (2010b) Noise from scattered light in Virgo's second science run data, *Class. Quantum Grav.* , **27**.

Campbell , K.W., (2009). Estimates of Shear-Wave Q and k_0 for Unconsolidated and Semiconsolidated Sediments in Eastern North America. *Bull. Seism. Soc. Amer.*, **99**, 23652392, *doi: 10.1785/0120080116.*

Cantini P., Testa G., Zanchetta G., Cavallini R. (2001) - The Plio-Pleistocene evolution of extensional tectonics in northern Tuscany, as constrained by new gravimetric data from the Montecarlo basin (lower Arno valley, Italy). *Tectonophysics*, **330**, 25-43.

Castagna, J. P., M. L. Batzle and R. L. Eastwood (1985). Relationships between compressional-wave and shear-wave velocities in clastic silicate rocks . *Geophysics*, **50**, 571-581.

Del Pezzo, E., G. Lombardo and S. Spampinato, (1989). Attenuation of Volcanic Tremor at Mt. Etna, Sicily. *Bull. Seism. Soc. Amer.*, **79**, 1989-1994.

Del Pezzo, E. and F. Giudicepietro, (2002) Plane wave fitting method for a plane, small aperture, short period seismic array: a MATHCAD 2000 professional program. *Computer and Geosciences* , **28**, 59-64.

Della Rocca B., Mazzanti R. e Pranzini E., (1988) - Studio geomorfologico della Pianura di Pisa. Geogr, Fis. Dinam. Quat., 10 (1987), 56-84.

Fanucci F., Firpo M., Ramella A. (1987) - Genesi ed evoluzione di piane costiere del Mediterraneo: esempi di piccole piane della Liguria. *Geogr. Fis. Dinam. Quat.*, **10**, 193-203

Fiori,I., L. Giordano, S. Hild, G. Losurdo, E.Marchetti, G. Mayer, and F.Paoletti (2009). A study of the seismic disturbance produced by the wind park near the gravitational wave detector GEO-600. Proc. $3^r d$ Int. Meeting on Wind Turbine Noise. Aalborg (Denmark), 1719 June 2009

Grassi S., Cortecci G., (2005) - Hydrogeology and geochemistry of the multilayered confined aquifer of the Pisa plain (Tuscany-central Italy). *Appl. Geochem.*, **20**, 41-54

Mariani M., Prato R. (1988) - I bacini neogenici costieri del margine tirrenico: approccio sismicostratigrafico. *Mem. Soc. Geol. It.*, **41**, 519-531

Mazzanti R. , Rau A (1994) - La Geologia. In: Mazzanti R. (ed.) - La pianura di Pisa e i rilievi contermini. La natura e la storia. *Mem. Soc. Geol. It.*, **50**, 31-87

Saulson P.R (1994) Interferometric gravitational wave detectors, *World Scientific*,316 ppgg.

Patacca E., Sartori R., Scandone P (1990) - Tyrrhenian basin and Apenninic arcs: kinematic relations since Late Tortonian times.*Mem. Soc. Geol. Ital.*, **45**, 425-451

Schofield R., (2001), Seismic Measurements at the Stateline Wind Project, LIGO T020104-00-Z.

Stefanelli P., Carmisciano C., Caratori Tontini F., Cocchi L., Beverini N., Fidecaro F. and D. Embriaco (2008) Microgravity vertical gradient measurement in the site of VIRGO interferometric antenna (Pisa plain, Italy). *Annals of Geoph.*, **51**, 877-886

Styles, P., (2005). A detailed study of the propagation and modelling of the effects of low frequency seismic vibration and infrasound from wind turbines. Proc. $1^s t$ Int. Meeting on Wind Turbine Noise, Berlin, Oct. 2005

Vinet, J.Y. et al. (1996) Scattered light noise in gravitational wave interferometric detectors: Coherent effects, *Phys. Rev. D*, **54**, 1276-1286

Welch, P. (1967). A direct digital method of power spectrum estimation, *IBM J. Res. Dev.*, **5**, 141.

Withers, M.M, R.C. Aster, C.J. Young and Eric P. Chael (1996). High-Frequency Analysis of Seismic Background Noise as a Function of Wind Speed and Shallow Depth . *Bull. Seism. Soc. Amer.*, **86**, 1507-1515

12 Figure Captions

Fig. 1 - Simplified Geological Map of Western Tuscany. The shaded region marks the area surrounding VIRGO and object of this study. The inset at the bottom-right shows the configuration of the VIRGO antenna (black lines), with location of the recording stations which have been kept fixed throughout the duration of the survey. Circles are Episensor accelerometers deployed at VIRGO's towers, and triangles are stations equipped with Guralp CMG-40T broad-band sensors. The square is the reference station 931E, equipped with a Lennartz LE3D-5s seismometer; stars mark the position of the four turbines of the windpark.

Fig. 2 - Spectrogram for the vertical component of ground velocity recorded at reference site 931E (see Fig. 1). Each spectrogram's column results from the average of spectral estimates obtained over 10 consecutive, not-overlapping 60-s-long windows of signal.

Unit is amplitude spectral density ($ms^{-1}/\sqrt{Hz}$), according to the color-bar at the right. Labels at the top of the map indicate days of the week.

Fig. 3 - Amplitude spectral density for the three component of ground velocity recorded at reference site 931E (see Fig.1) during night- and day-time periods (gray and black lines, respectively), both in absence of wind. Spectral densities are obtained using 10 consecutive, not-overlapping 600-s-long windows of signal. The bottom panel reports the spectral ratios between day- and night-time measurements.

Fig. 4 - *(a)* Maxima of the Cross-Correlation function between narrow band noise amplitude and wind speed. *(b)*: Time lags associated with correlation coefficients greater than 0.4. *(c)* Time evolution of the seismic noise

amplitude at frequency 1.7 Hz (NS component of reference site 931E) and wind speed recorded at EGO's premise.

Fig. 5 - Time series (top) and corresponding spectrogram (bottom) for the vertical component of ground velocity observed at the base of a turbine, and encompassing a switch-on sequence ($\approx$ 3100 s into the record).

Unit is amplitude spectral density $(ms^{-1}/\sqrt{Hz}$, according to the grayscale at the right.

Fig. 6 - Comparison of spectral amplitudes observed beneath a turbine and at reference site 931E (black and gray lines, respectively). The two data set are not simultaneous, and correspond to wind speed of $\approx$ 3 m/s and $\approx$ 11 m/s, respectively.

Fig. 7 - *(a)* Dispersion curve, derived from the frequency-dependent slowness estimates. Slowness data are obtained from 24 consecutive, not-overlapping 600-s-long time windows. The inset shows the configuration of the array used for slowness estimates (circles), with respect to the wind park (stars). *(b)* Wave Backazimuth (direction-of-arrival) as a function of frequency. The two dashed lines mark the angular interval encompassing the wind park.

Fig. 8 - *(a)* Spatial decay of the amplitude of ground velocity (N component) for increasing distance from the barycenter of the windpark. The image map is the logarithm of the amplitude spectral density $(ms^{-1}/\sqrt{(}Hz))$, according to the colorbar at the top. The peak at frequency 1.7 Hz is clearly observed at VIRGO's west end, $\approx$ 11 km from the wind park. *(b)* Spatial decay of the amplitude at the frequency 1.7 Hz. The decay rate changes abruptly for distances on the order 2500–3000 m, suggesting the emergence

of waves which propagated through deeper paths.

Fig. 9 - Sketch of the propagation model used for interpreting amplitude data. Seismic waves radiated from a source at the surface propagate as both surface waves and body head waves refracted at a deep interface; XC is the critical distance. Surface waves are entirely confined within the shallowest layer, while body waves propagate through a layer of thickness h and at the interface between this layer and an halfspace represented by the carbonate basement. Shear-wave velocities and quality factors are listed within each layer.

Fig. 10 - *(a)* L_1-norm misfit function obtained from the regular grid-search over the parameters A_0 and n for fitting equation 3 to three-component amplitude data. *(b)* Fit of experimental, three-component amplitudes using the best values of the parameters obtained from the minimum of the misfit function in *(a)*

Fig. 11 - Relationships between vibration amplitude at a single turbine and wind speed. Gray tones indicate wind directions measured clockwise from North, according to the gray scale at the right.

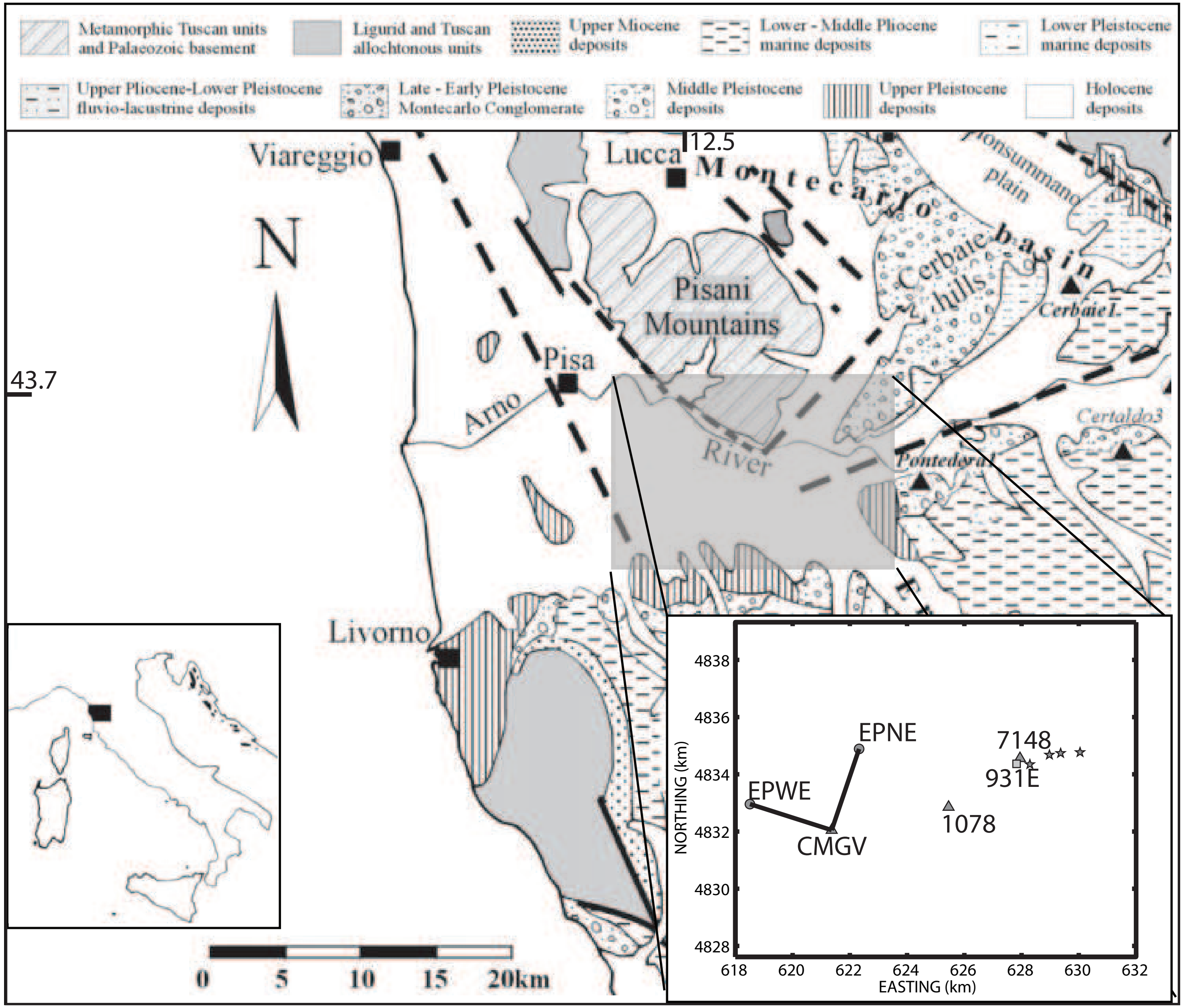
Metamorphic Tuscan units and Palaeozoic basement
Ligurid and Tuscan allochtonous units
Upper Miocene deposits
Lower - Middle Pliocene marine deposits
Lower Pleistocene marine deposits
Upper Pliocene-Lower Pleistocene fluvio-lacustrine deposits
Late - Early Pleistocene Montecarlo Conglomerate
Middle Pleistocene deposits
Upper Pleistocene deposits
Holocene deposits
Viareggio
Lucca
12.5
Montecarlo
Monsummano plain
Cerbaie basin
Cerbaie hills
Cerbaie1
Pisani Mountains
N
Pisa
43.7
Arno
River
Certaldo3
Pontedera
Livorno
0 5 10 15 20km
NORTHING (km)
EASTING (km)
EPNE
EPWE
CMGV
7148
931E
1078
4828
4830
4832
4834
4836
4838
618
620
622
624
626
628
630
632

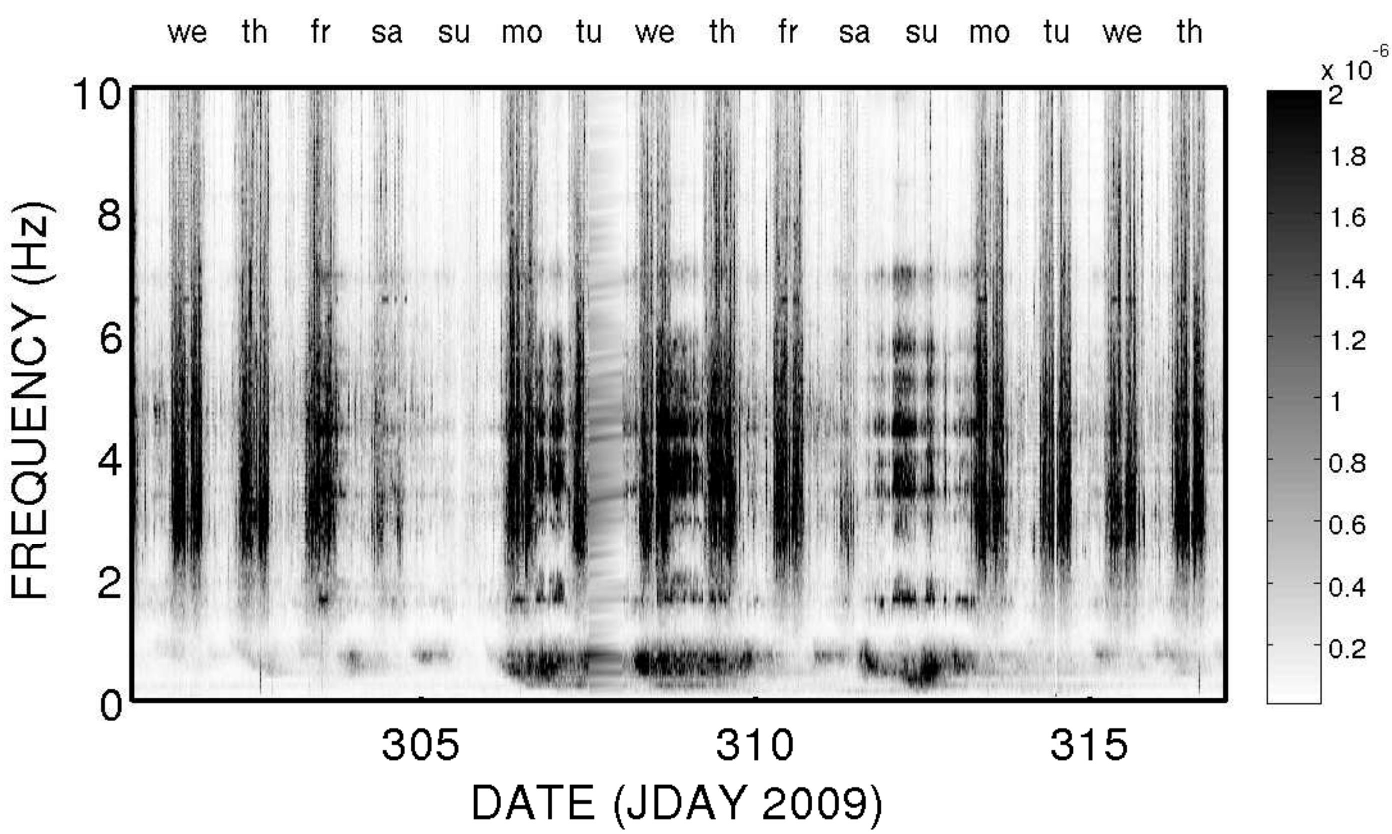

we th fr sa su mo tu we th fr sa su mo tu we th
FREQUENCY (Hz)
0
2
4
6
8
10
305
310
315
DATE (JDAY 2009)
x 10^-6
0.2
0.4
0.6
0.8
1
1.2
1.4
1.6
1.8
2

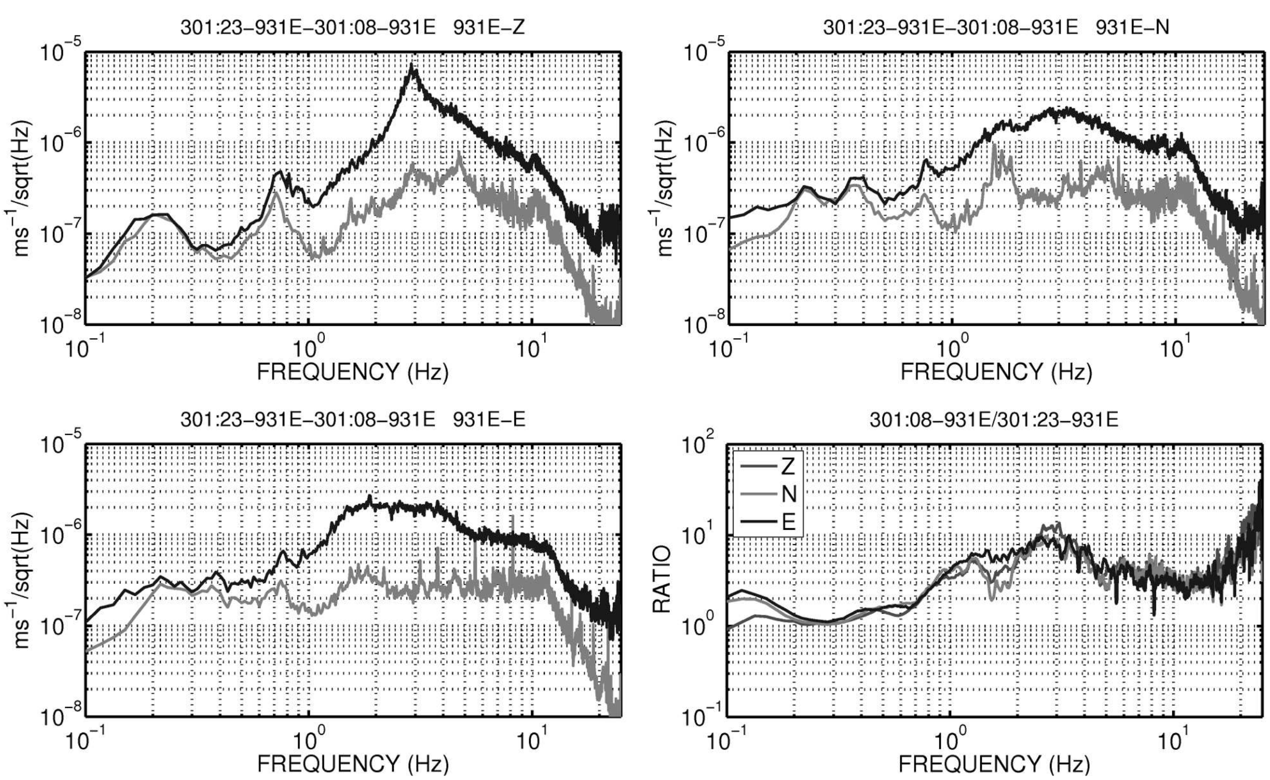

301:23−931E−301:08−931E 931E−Z
301:23−931E−301:08−931E 931E−N
301:23−931E−301:08−931E 931E−E
301:08−931E/301:23−931E
ms^{-1}/sqrt(Hz)
RATIO
FREQUENCY (Hz)
Z
N
E

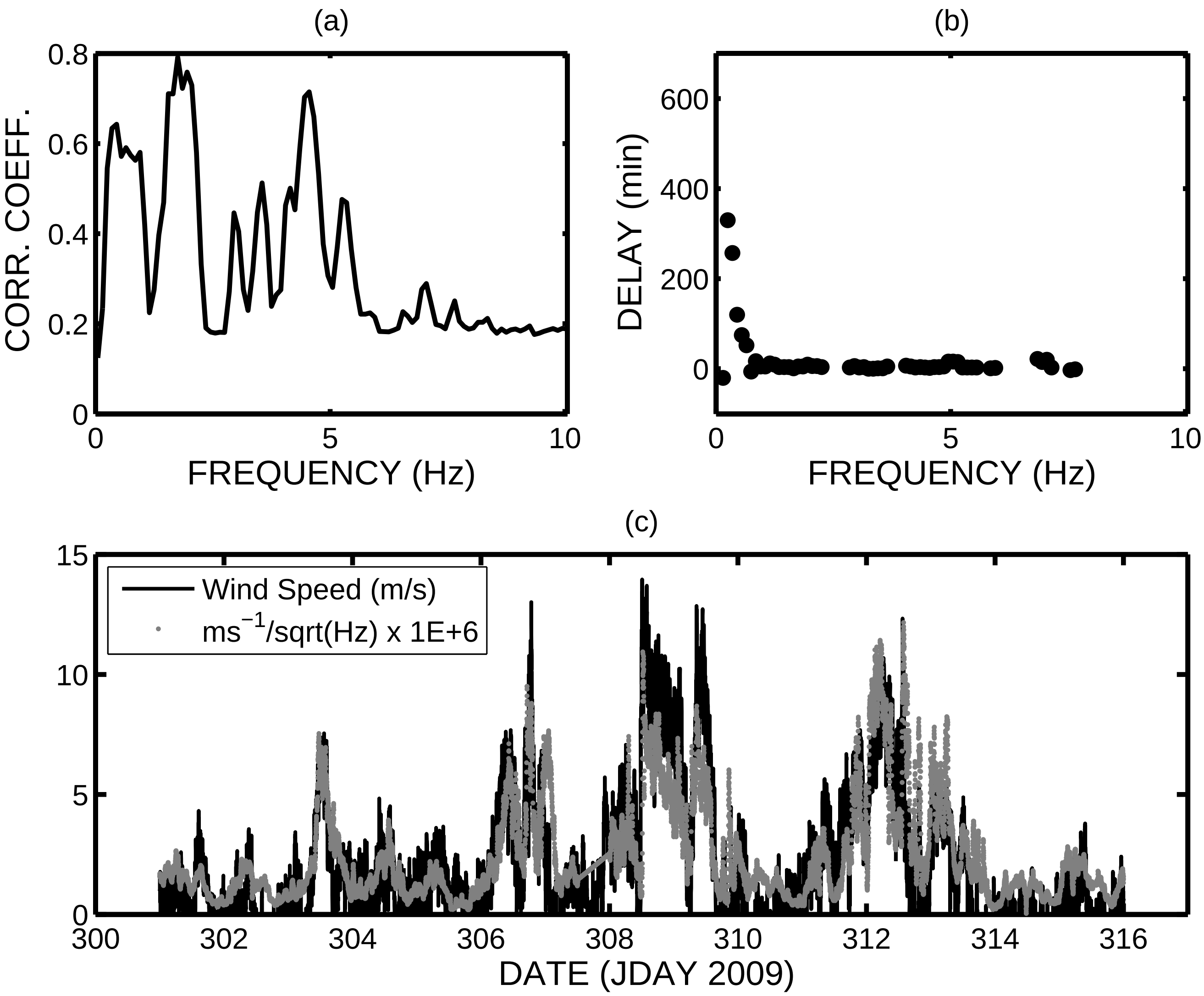
(a)
0.8
0.6
0.4
0.2
0
CORR. COEFF.
0
5
10
FREQUENCY (Hz)
(b)
600
400
200
0
DELAY (min)
0
5
10
FREQUENCY (Hz)
(c)
15
10
5
0
Wind Speed (m/s)
ms^{-1}/sqrt(Hz) x 1E+6
300
302
304
306
308
310
312
314
316
DATE (JDAY 2009)

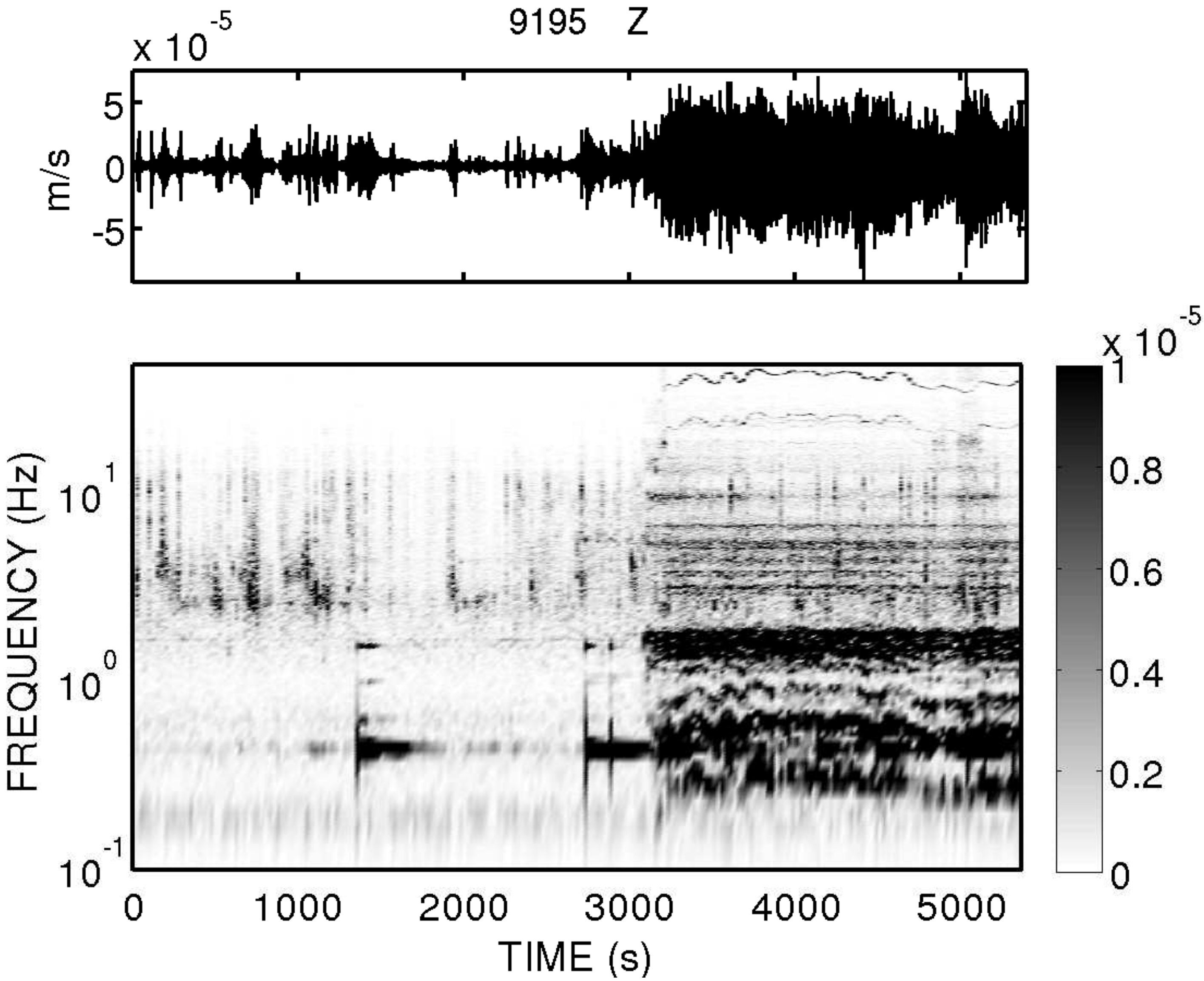
9195 Z
x 10^-5
m/s
5
0
-5
FREQUENCY (Hz)
10^1
10^0
10^-1
x 10^-5
1
0.8
0.6
0.4
0.2
0
0
1000
2000
3000
4000
5000
TIME (s)

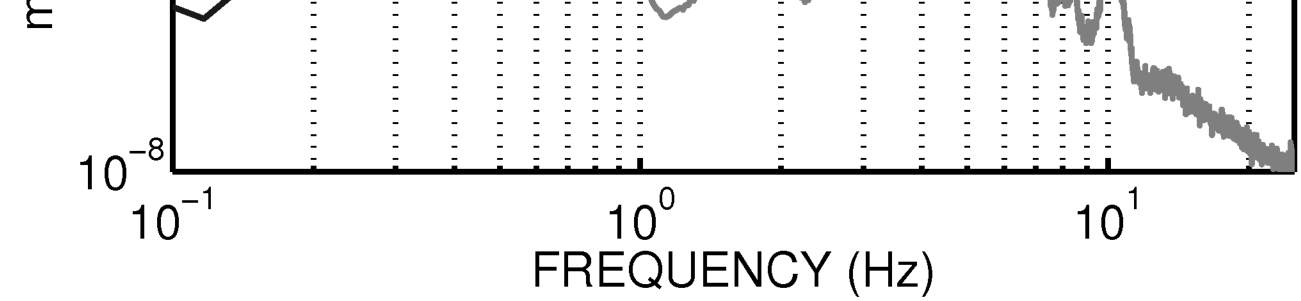

10^−8
10^−1
10^0
10^1
FREQUENCY (Hz)

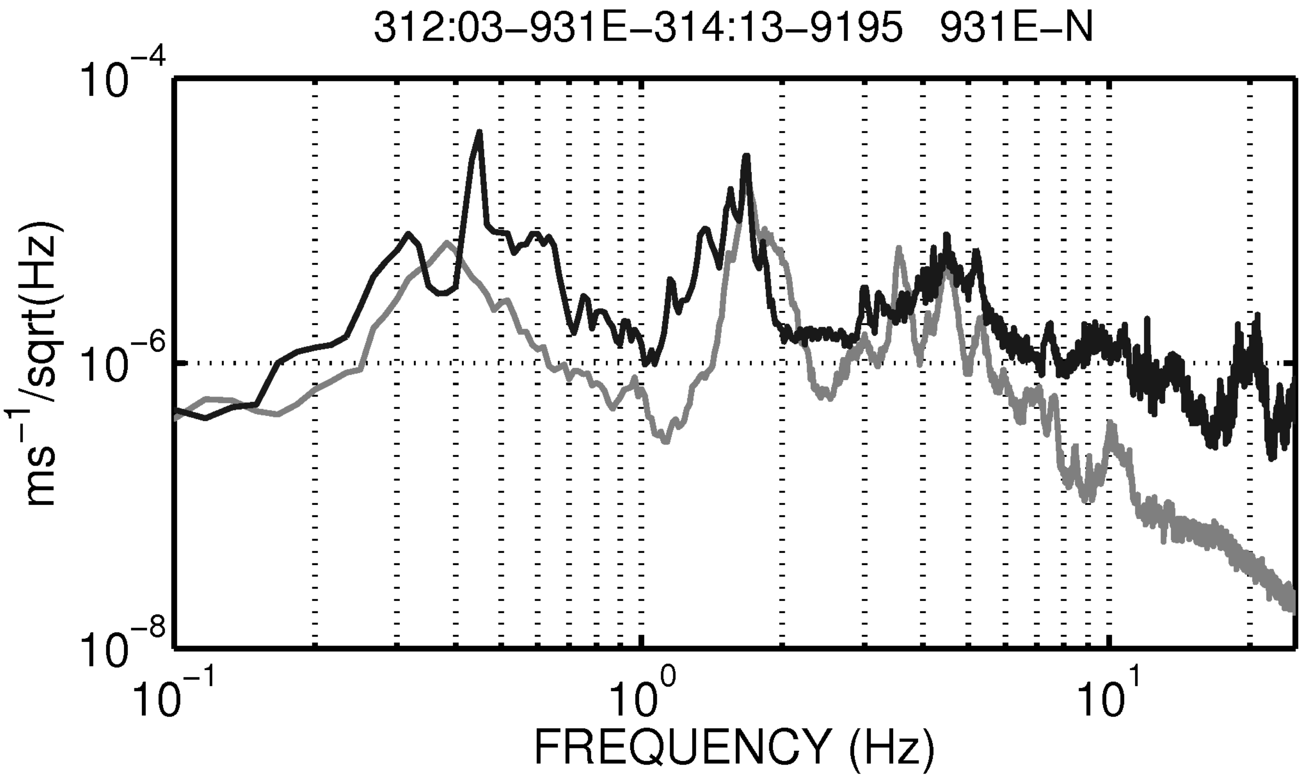

312:03−931E−314:13−9195 931E−N
10^−4
10^−6
10^−8
ms^−1/sqrt(Hz)
10^−1
10^0
10^1
FREQUENCY (Hz)

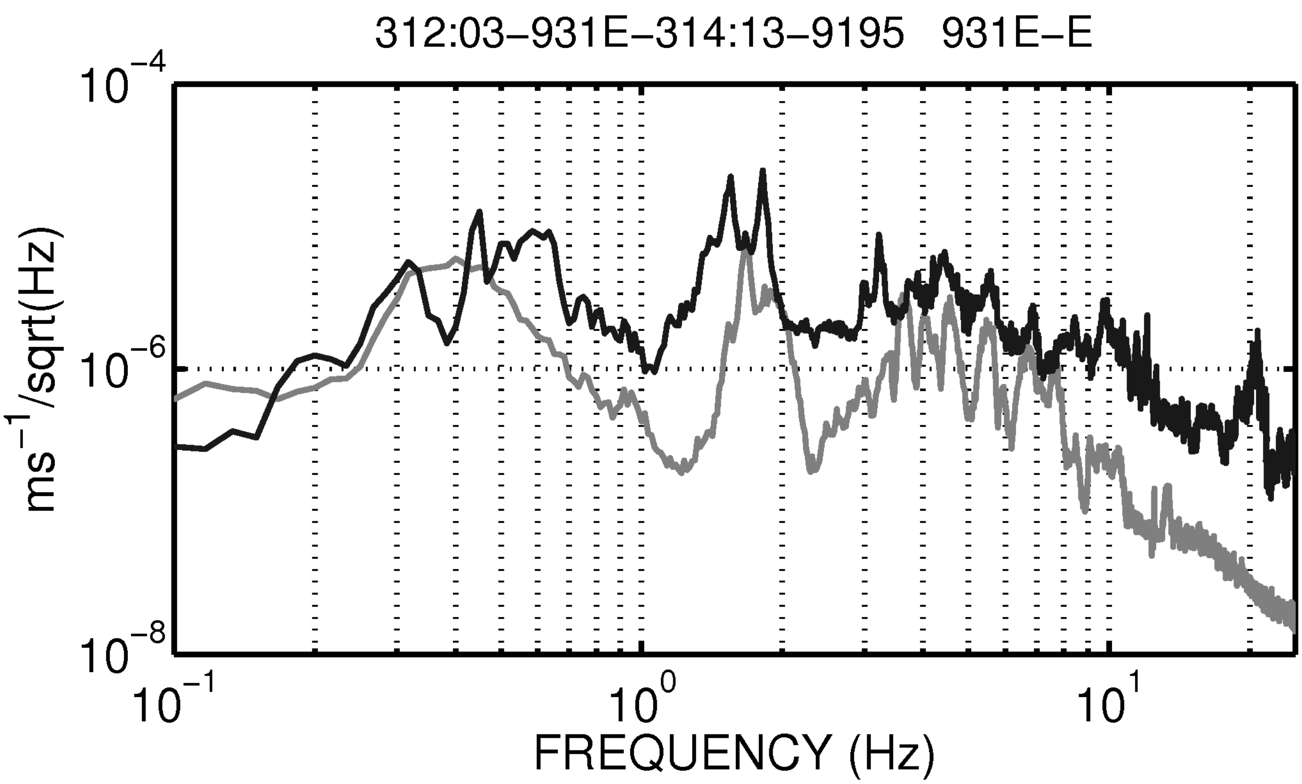

312:03−931E−314:13−9195 931E−E
10^−4
10^−6
10^−8
ms^−1/sqrt(Hz)
10^−1
10^0
10^1
FREQUENCY (Hz)

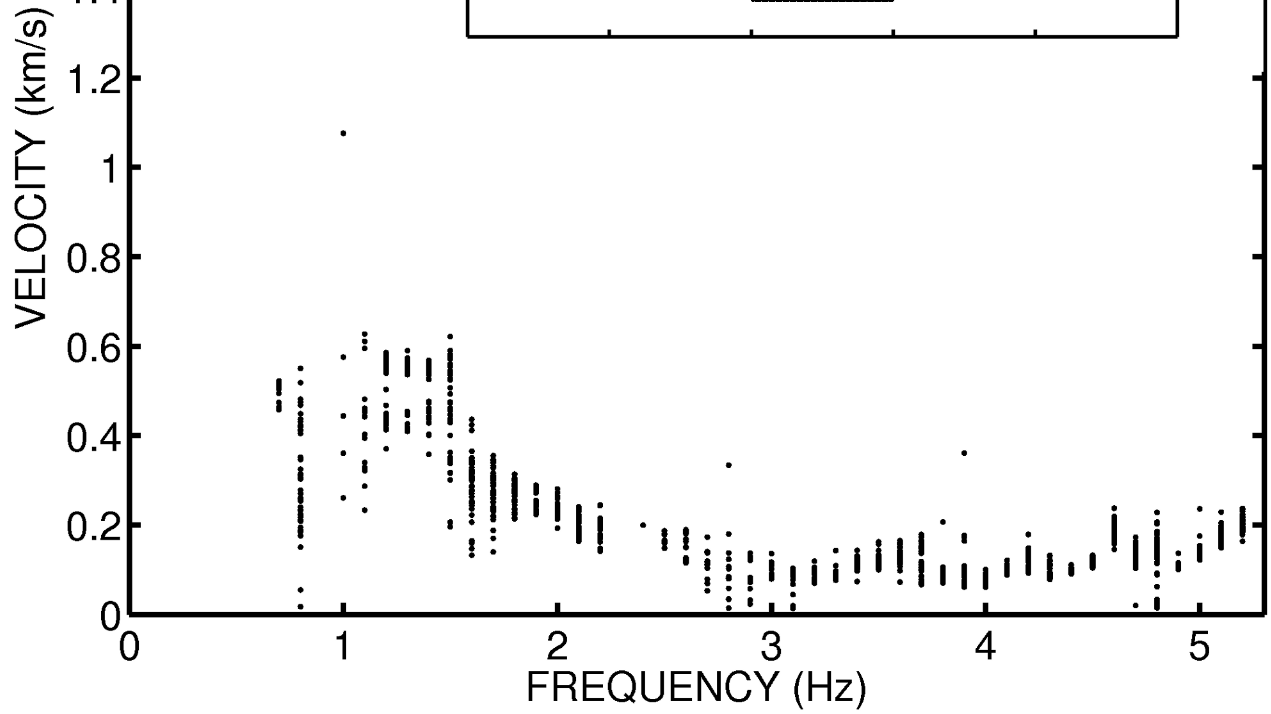
VELOCITY (km/s)
1.2
1
0.8
0.6
0.4
0.2
0
0
1
2
3
4
5
FREQUENCY (Hz)

DOA

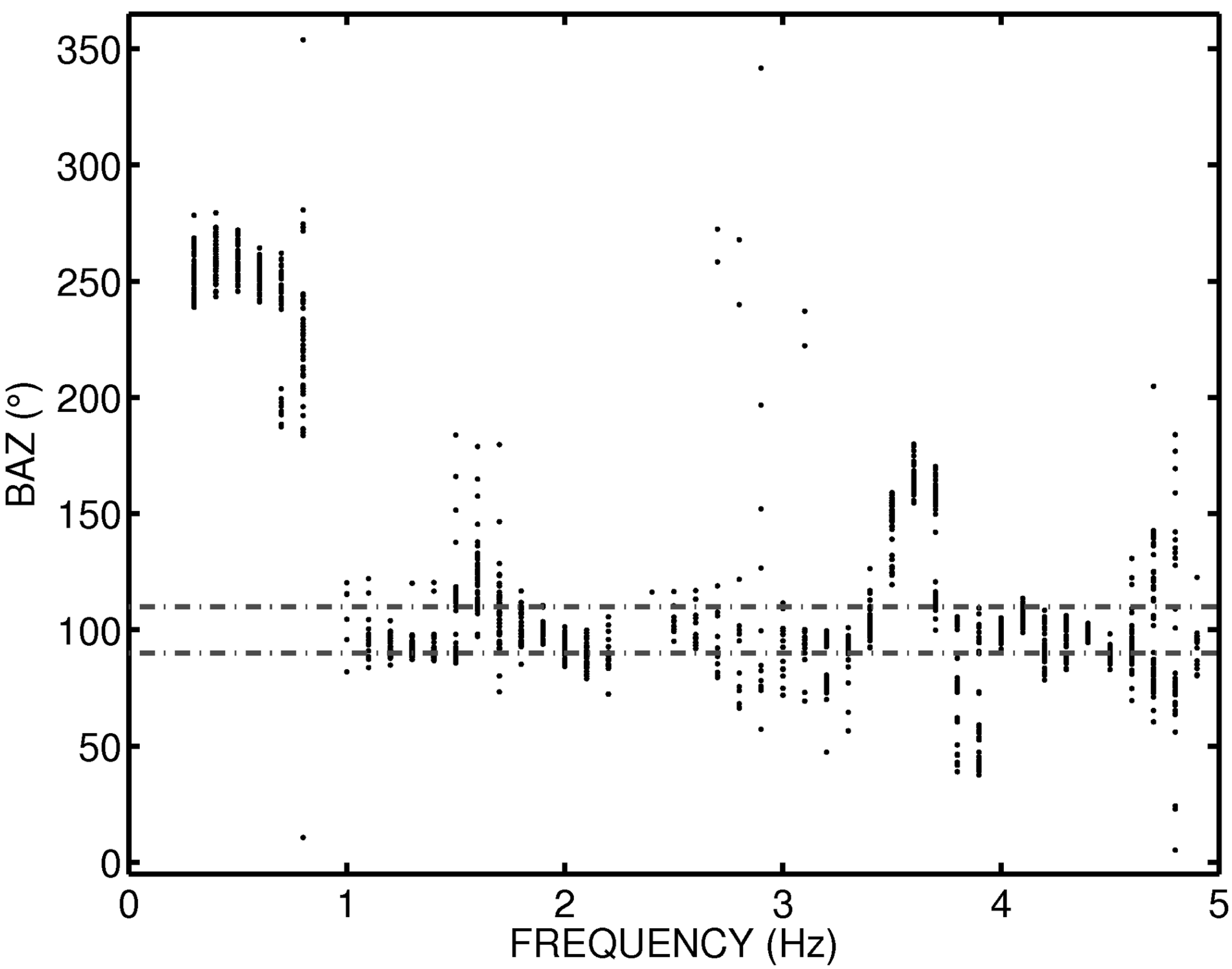
BAZ (°)
350
300
250
200
150
100
50
0
0
1
2
3
4
5
FREQUENCY (Hz)

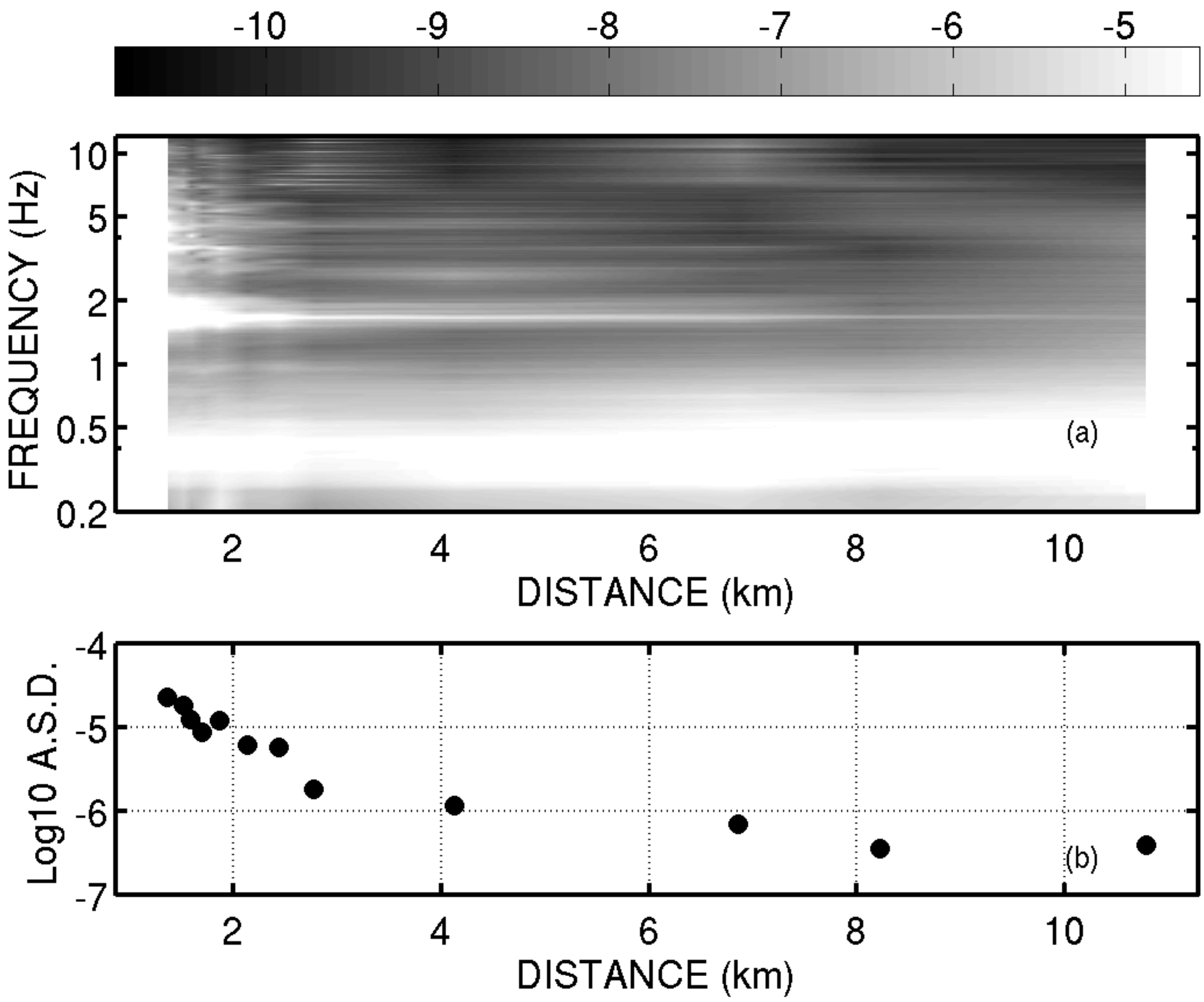
-10
-9
-8
-7
-6
-5
FREQUENCY (Hz)
10
5
2
1
0.5
0.2
(a)
2
4
6
8
10
DISTANCE (km)
Log10 A.S.D.
-4
-5
-6
-7
(b)
2
4
6
8
10
DISTANCE (km)

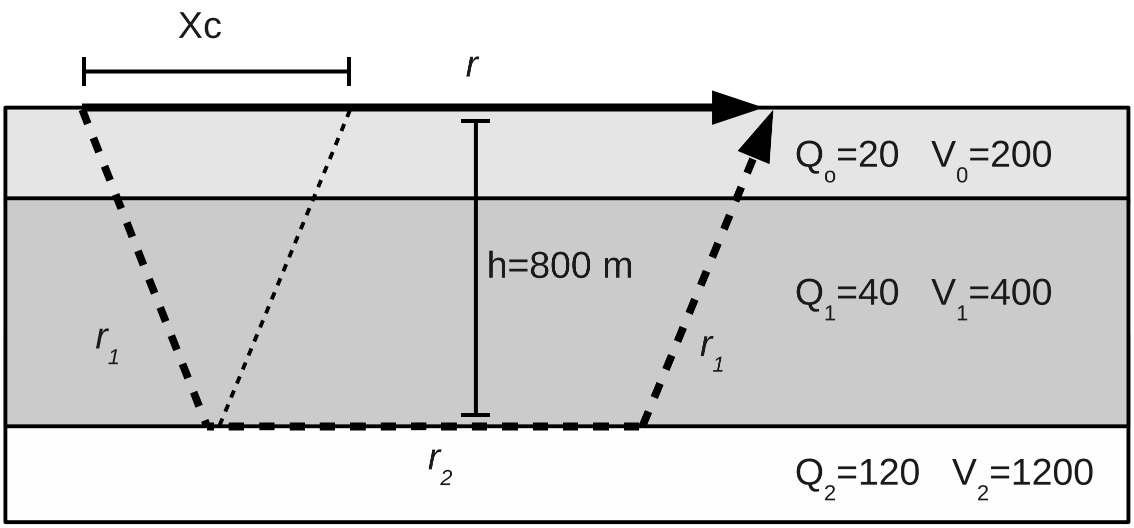

Xc
r
Qo=20 V0=200
h=800 m
Q1=40 V1=400
r1
r1
r2
Q2=120 V2=1200

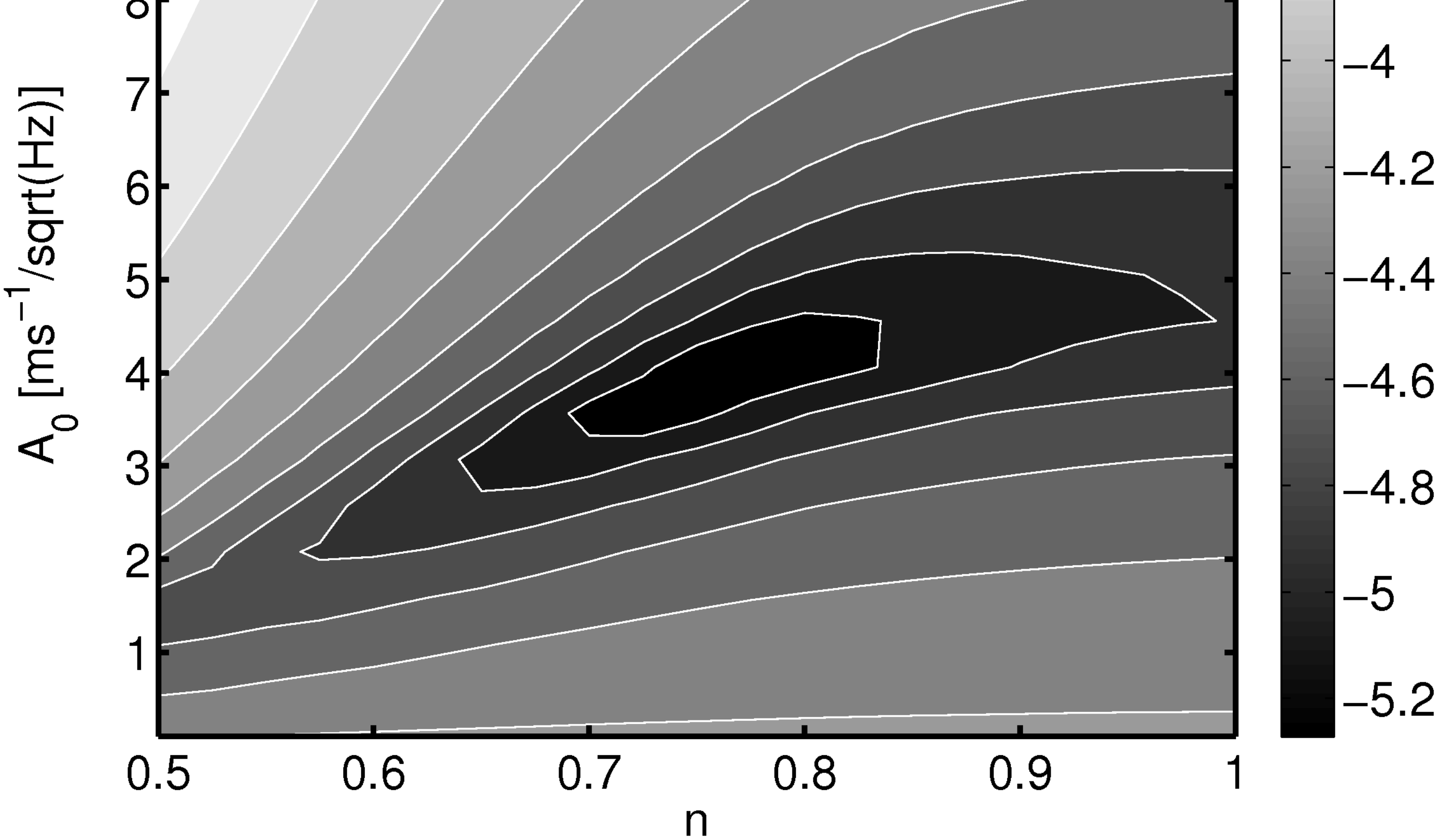

A_0 [ms^-1/sqrt(Hz)]
n
0.5
0.6
0.7
0.8
0.9
1
1
2
3
4
5
6
7
8
−4
−4.2
−4.4
−4.6
−4.8
−5
−5.2

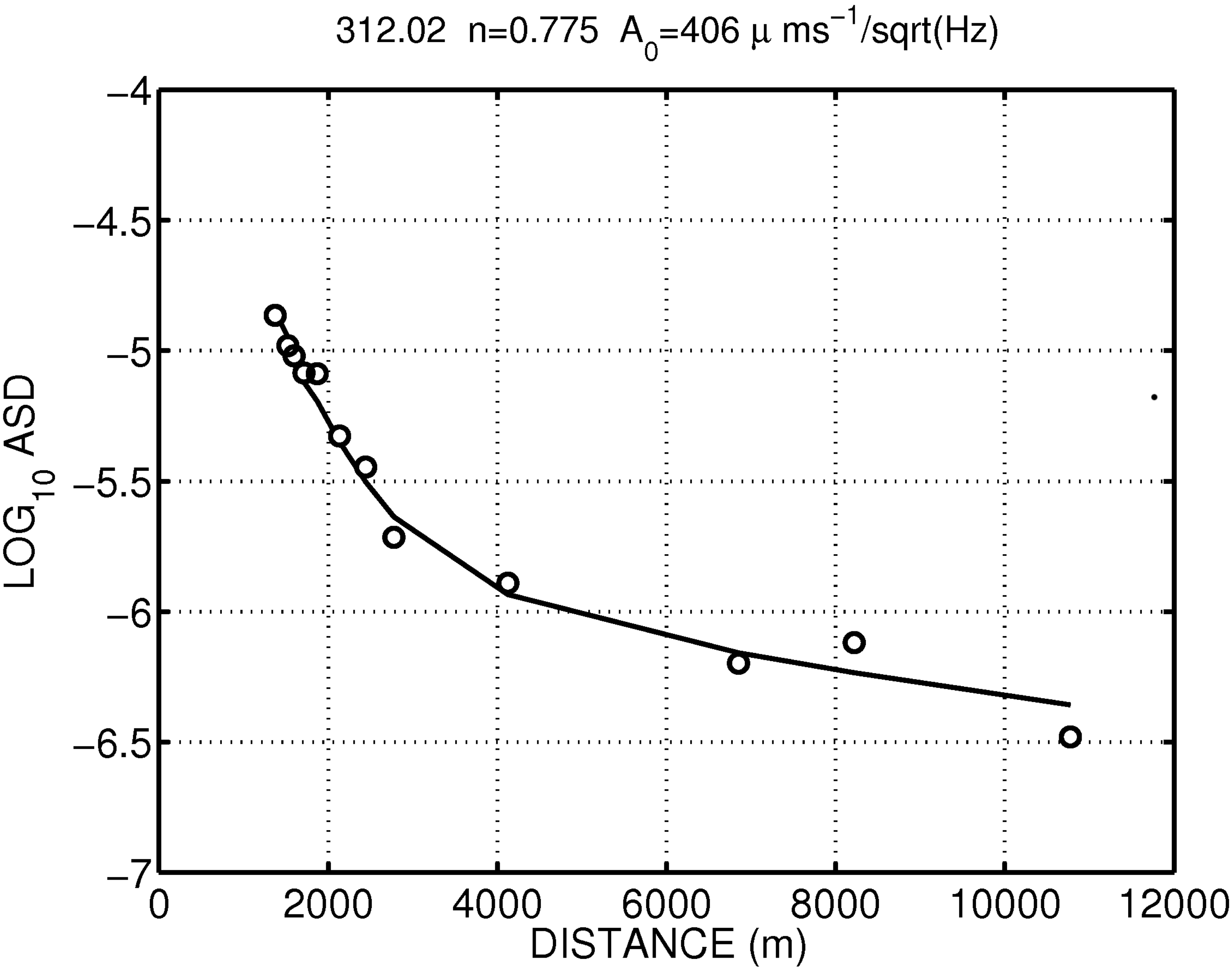

312.02 n=0.775 A_0=406 μ ms^-1/sqrt(Hz)
LOG_10 ASD
DISTANCE (m)
−4
−4.5
−5
−5.5
−6
−6.5
−7
0
2000
4000
6000
8000
10000
12000

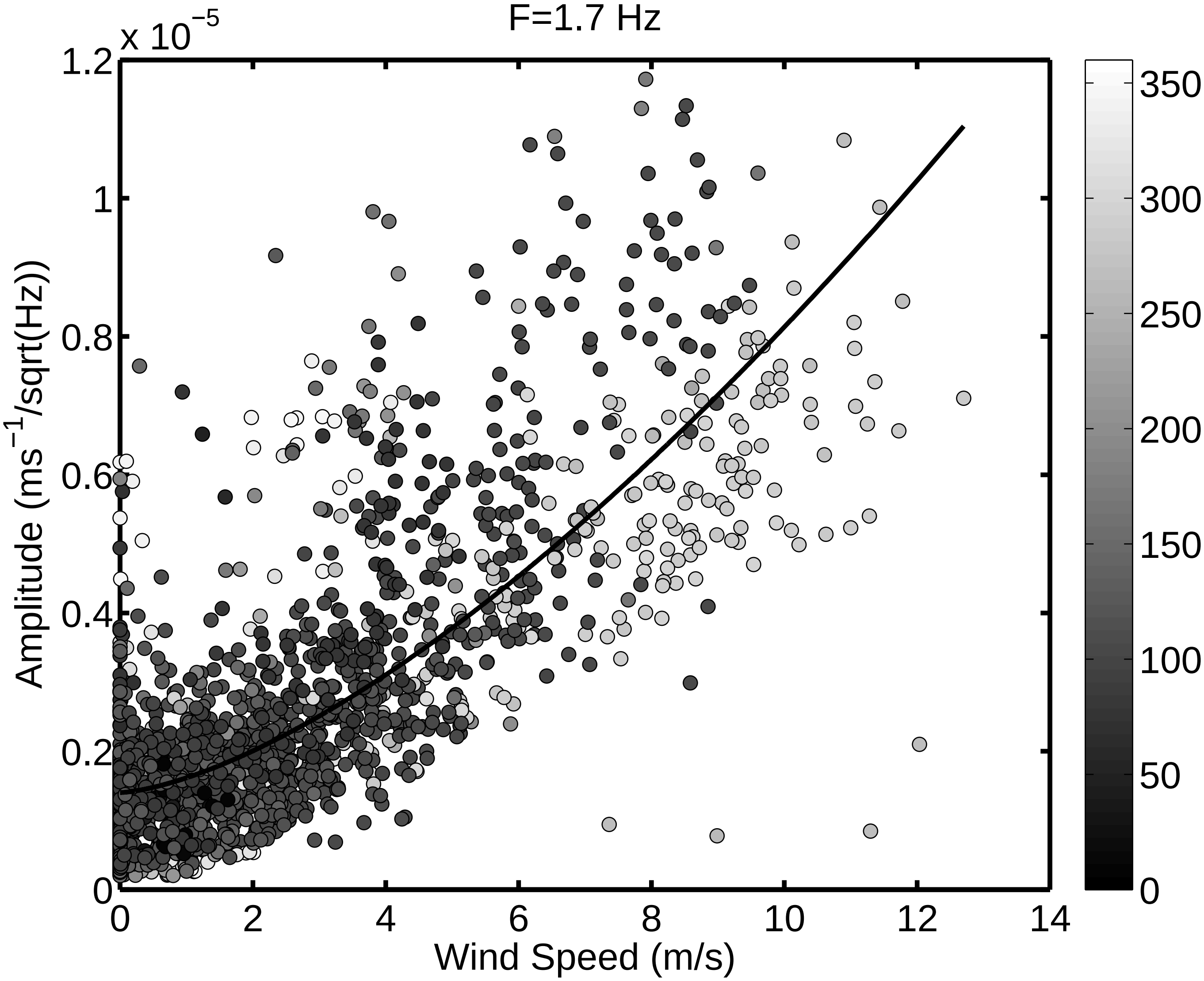
F=1.7 Hz
x 10^−5
Amplitude (ms^−1/sqrt(Hz))
Wind Speed (m/s)
0
0.2
0.4
0.6
0.8
1
1.2
0
2
4
6
8
10
12
14
0
50
100
150
200
250
300
350